

## Temporal variability and estimation of jet parameters for Ton 599

S. R. PATEL,<sup>1,2</sup> V. R. CHITNIS,<sup>1</sup> A. SHUKLA,<sup>3</sup> A. R. RAO,<sup>4</sup> AND B. J. NAGARE<sup>2</sup>

<sup>1</sup>*Department of High Energy Physics, Tata Institute of Fundamental Research, Homi bhabha road, Mumbai-400005, India*

<sup>2</sup>*Department of Physics, University of Mumbai, Santacruz (E), Mumbai-400098, India*

<sup>3</sup>*Institute for Theoretical physics and Astrophysics, Universität Würzburg, 97074 Würzburg, Germany*

<sup>4</sup>*Department of Astronomy and Astrophysics, Tata Institute of Fundamental Research, Homi bhabha road, Mumbai-400005, India*

(Received; Revised; Accepted)

Submitted to ApJ

### ABSTRACT

The TeV blazar Ton 599 has exhibited a peculiar flare in 2017 November. The temporal variation of the source is studied using simultaneous  $\gamma$ -ray data from *Fermi* Large Area Telescope and radio data from Owens Valley Radio Observatory's 40 m telescope, over the period of nine years. Four major flaring periods are observed in the  $\gamma$ -ray energy band of 0.1-300 GeV. These periods are studied on a shorter timescale and modeled with a time-dependent function containing exponential rising and decaying components. The physical parameters of the jet are estimated numerically and compared with those reported in the literature. During the fourth flare a bunch of high energy photons ( $> 10$  GeV) were detected. The two highest energy photons having an

energy of 76.9 GeV and 61.9 GeV are detected on MJD 58059.0 and 58073.3, respectively. This observation possibly constrains the  $\gamma$ -ray emission region to lie near outer edge or outside the broad line region of size  $\sim 0.08$  pc. The variation of equivalent width of a Mg-II line is studied using the spectroscopic data from Steward observatory. It was observed that the equivalent width of the line varies inversely with the underlying power-law continuum.

*Keywords:* Gamma rays: general – Quasar: emission lines – Quasar: individual (Ton 599) – Radiation mechanisms: non-thermal

## 1. INTRODUCTION

Blazars are a subclass of active galactic nuclei (AGNs), characterized by a significant variability at all wavelengths and with the flux variation timescale ranging from minutes to years. The variability carries plenty of information about the structure and energy changes happening at the center of the source. The emission from blazars is generally thought to be coming from the relativistic jets which are beamed towards the observer (Urry & Padovani 1995). Blazars are classified into two categories based on the observation of the optical spectra, as BL Lacertae (BL Lac) and flat spectrum radio quasars (FSRQ). The BL Lac has a featureless optical spectrum while the FSRQ shows characteristic strong emission lines in an optical spectrum.

The FSRQ, Ton 599 ( $z=0.725$ , Schneider et al. 2010; Hewett & Wild 2010) shows significant variability across the entire electromagnetic spectrum from radio to  $\gamma$ -rays. Owing to the wide range of variability, Ton 599 has been studied since more than four decades in several energy bands. At  $\gamma$ -ray energies, it was detected in the second EGRET catalog (Thompson et al. 1995). Due to better sensitivity of Large Area Telescope on board *Fermi* satellite (*Fermi*-LAT), this source was detected in the first three months of operation (Abdo et al. 2010a). During the period 1992 to 1996, three strong flares having flux of  $\sim 3.9 \times 10^{-10}$  Jy ( $\sim 9.4 \times 10^{-11}$  erg cm $^{-2}$  s $^{-1}$ ) were detected at energies  $> 100$  MeV by EGRET (Thompson et al. 1995; Mukherjee et al. 1997; Hartman et al. 1999).

The blazars are known to show aperiodic variability. Also claims of periodicity in radio band have been reported for several blazars, for example, A0 0235+16 (Raiteri et al. 2001; Liu et al. 2006a), PKS 1510-089 (Xie et al. 2008), NRAO 530 (An et al. 2013), OJ 287 (Sillanpaa et al. 1988; Valtaoja et al. 2000; Cohen 2017) and PKS 0219-164 (Bhatta 2017). Ton 599 was regularly monitored by University of Michigan Radio Astronomy Observatory (UMRAO, Aller et al. 1985). The weekly sampled data collected over nearly 33 years upto 2012, were used to search for a characteristic periodic variability of the source (Liu & Liu 2014). This object also exhibited a possible quasi periodic oscillation having period of  $\sim 2.3 \pm 0.1$  years in the radio band (Wang et al. 2014; Liu & Liu 2014). The data collected between 2010–2013 from RATAN–600 radio telescope (Special Astrophysical Observatory, Russian Academy of Sciences, Gorshkov & Khromov (1981); Gorshkov et al. (2003)) and 32 m Zelenchuk and Badary radio telescope (Gorshkov et al. 2009), were used to search for intra day variability (IDV). The IDV timescale of 6 h at 4.85 GHz was detected on November 10-11, 2012 at the Badary station (Gorshkov et al. 2014). The flux density variation of 40 % on timescale of 2.7 h was observed during 2007 February 5 by the MOJAVE survey program (Lister & Homan 2005) with the VLBA at 15 GHz, which had placed this source in between classical IDV and intra-hour variable sources (Savolainen & Kovalev 2008).

Ton 599 is classified as an optically violent variable and a highly polarized quasar (Wills et al. 1983; Fan et al. 2006). A long-term study of this source in the optical bands (Johnson V, Cousins RI passbands) was carried out for the data collected from 1997 April to 2002 March, using 1.56 m telescope of the Shanghai Astronomical Observatory at Sheshan, China, by Fan et al. (2006). They searched for a possible periodicity in the lightcurve and the periods of 1.58 and 3.55 years were reported. The periodic variation consisting of two outbursts having one-year-separating double-peaked structure with a gap of 3.2 years in the infrared (JHK band) was also reported by Fan (1999) using the historic data compiled from literature.

The connection between the  $\gamma$ -ray and radio emissions has also been studied for this source and constraints are put on  $\gamma$ -ray emitting region in parsec-scale jet by Ramakrishnan et al. (2014). They interpreted, using radio data, the identification of four moving components and one stationary

component as the complex change in the jet structure due to formation of a trailing shock in an inner region of the jet. A radiative transfer model (Hughes et al. 2011), was used for this source in order to reproduce the observed lightcurve (Aller et al. 2014) and the linear polarization. The helical jet model was also used for this source to explain a "double-peak" structure of the total flux density lightcurve by Hong et al. (2004) in radio band. They infer that the double-peak structure should appear, if the jet components always travel along the helical path aligned with the line of sight of the observer.

In the present work, a long-term temporal study of the FSRQ Ton 599 in  $\gamma$ -ray energy band is carried out and the jet parameters are estimated. We identified four major outbursts in this energy band since 2008. The source is then studied in detail at four epochs during which outbursts occurred. Also the possible implication of the time lag between  $\gamma$ -ray and radio emission is discussed. The variation of the Mg-II line with underlying continuum is studied to see the effect of different flux states on the broad line region (BLR). The observations and analysis of the data used in this work is discussed in Section 2 and results of the analysis are mentioned in Section 3. In Section 4, the spectral energy distributions (SEDs) at four different epochs are discussed and we conclude our work with a discussion in Section 5 and a conclusion in Section 6. A flat  $\Lambda$ -CDM cosmology with  $H_0 = 69.6 \text{ km s}^{-1} \text{ Mpc}^{-1}$ ,  $\Omega_m = 0.286$ , and  $\Omega_\Lambda = 0.714$  is used in this work (Planck Collaboration et al. 2014).

## 2. OBSERVATIONS AND DATA ANALYSIS

In this study, the high energy  $\gamma$ -ray data from *Fermi*-LAT was obtained for the period of around nine years. The publicly available spectroscopic data from SPOL and radio data from OVRO were used in this work. Also X-ray and Optical-UV data were taken from X-ray telescope on board *Swift* satellite (*Swift*-XRT). In this section, we describe these data sets and an analysis procedure used in this work.

### 2.1. High energy $\gamma$ -ray observations from *Fermi*-LAT

The *Fermi*-LAT (Atwood et al. 2009) is a pair-conversion  $\gamma$ -ray telescope operational since 2008. It has a large field of view of  $2.4\text{ sr}$ , because of which it scans the whole sky in  $\sim 3$  hours period. The Science Tools version v10r0p5 and user contributed *enrico* software (Sanchez & Deil 2013) were used for analysis of Ton 599 data. The *Fermi*-LAT data<sup>1</sup> in the energy range of 0.1 - 300 GeV were collected during 2008 August 22 (MJD 54700) to 2018 May 22 (MJD 58260) period. For analysis, the events were extracted from the region of interest (ROI) of  $15^\circ$  centered around the source position (RA=179.883, Dec.=29.2455). In order to avoid the contamination of the background  $\gamma$ -rays from Earth's limb, zenith angle cut of  $90^\circ$  was applied. A filter of '(DATA\_QUAL>0)&&(LAT\_CONFIG==1)' was applied to select the good time intervals. The unbinned likelihood analysis was performed using *glike* (Cash 1979; Mattox et al. 1996). Our model contained 66 point sources from 3FGL catalog. The parameters of sources within  $5^\circ$  region around the source were left free to vary. Also the parameters of one bright source J1224.9+2122,  $\sim 9^\circ$  away from Ton 599 were kept free. The likelihood analysis was performed iteratively by removing the source having significance less than  $1\sigma$  after each fit. Our source was modeled with a power law spectrum for the lightcurves. In the analysis the galactic diffuse emission and the isotropic background were modeled using "gll\_iem\_v06.fit" and "iso\_P8R2\_SOURCE\_V6\_v06.txt", respectively with the post launch instrument response function (P8R2\_SOURCE\_V6). The fluxes were obtained with integration time of one day, two days and ten days depending on the science goals, with detection criterion such as maximum likelihood test statistics (TS; Mattox et al. 1996) exceeding 9 ( $\sim 3\sigma$ ). For fluxes with the detection of  $TS < 9$ , the upperlimit at 0.95 confidence level were estimated using the profile likelihood method (Rolke et al. 2005). To obtain the probability of photons with energy above 10 GeV, being associated with Ton 599, within  $0.5^\circ$ , *gtsrcprob* was used. This tool is provided with the *Fermi* science tools.

<sup>1</sup> <https://fermi.gsfc.nasa.gov/ssc/data/>

The spectra were obtained during four epochs, when the source was in the high flux state and a fitting was performed using maximum likelihood analysis. The functions used for fitting are as follows,

1. A Power-law (PL), defined as

$$dN(E)/dE = N_0(E/E_p)^{-\Gamma}, \quad (1)$$

where,  $E_p=439.38$  MeV, which is the value of pivot energy given in 3FGL catalog and  $\Gamma$  is the spectral index.

2. A broken power-law (BPL), defined as

$$dN(E)/dE = N_0(E/E_{break})^{-\Gamma_i}, \quad (2)$$

with  $i = 1$  if  $E < E_{break}$  and  $i = 2$  if  $E > E_{break}$ ,  $\Gamma_1$  and  $\Gamma_2$  are the spectral indices before and after the break energy,  $E_{break}$ , respectively.

3. A log-parabola (LP), defined as

$$dN(E)/dE = N_0(E/E_0)^{-(\alpha+\beta\log(E/E_0))}, \quad (3)$$

where,  $E_0$  is the value of the pivot energy (same as PL),  $\alpha$  and  $\beta$  are the spectral index and curvature parameter, respectively.

4. A Power-law with an exponential cutoff (PLEC), defined as

$$dN(E)/dE = N_0(E/E_p)^{-\Gamma_{PLEC}} \exp(-E/E_c), \quad (4)$$

where  $E_p$  is the value of pivot energy (same as PL).  $\Gamma_{PLEC}$  is the spectral index and  $E_c$  is the value of cutoff energy.  $N_0$  is the normalization parameter for all the models.

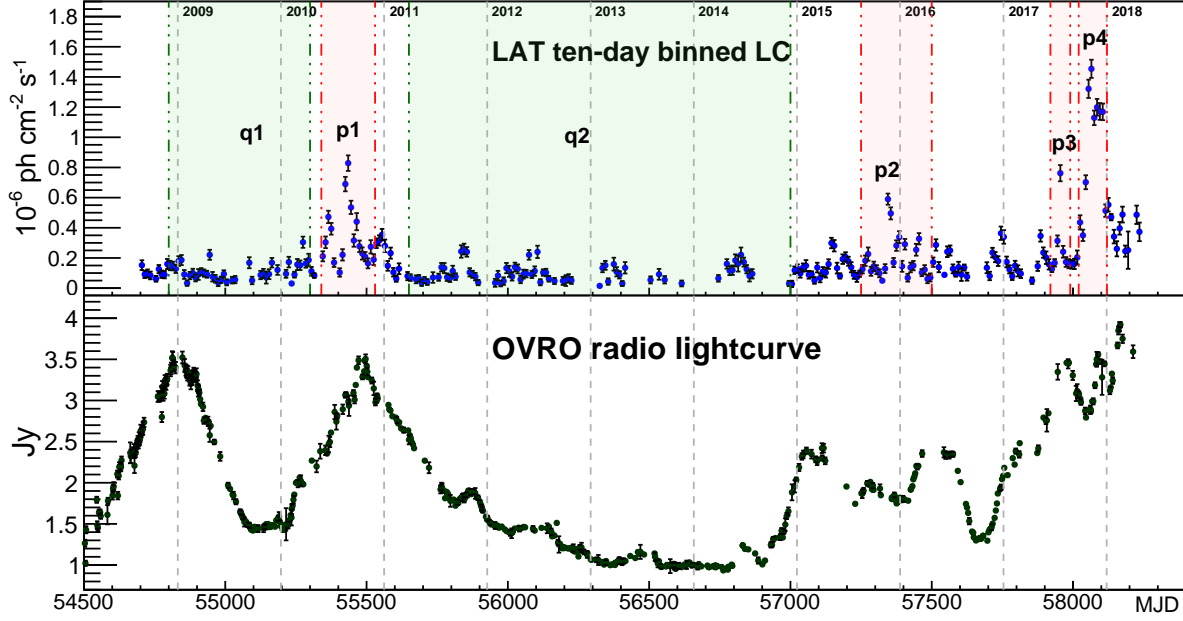


**Figure 1.** Nine years lightcurve of Ton 599 from MJD 54700 - 58260, *Panel-1* : Ten days binned 0.1 - 300 GeV flux in  $10^{-6}$  ph  $\text{cm}^{-2}\text{s}^{-1}$ , *Panel-2* : Radio flux density at 15 GHz in Jy; The shaded regions between two red dot-dashed lines correspond to the periods which are studied in detail and marked as p1, p2, p3, and p4. The shaded periods between two green dot-dashed lines, marked as q1 and q2 correspond to quiescent states of the source. The gray dashed lines correspond to start of the year.

## 2.2. X-ray observations from *Swift*-XRT

The soft X-ray data<sup>2</sup> in the energy range of 0.3 - 8 keV were obtained from *Swift*-XRT (Burrows et al. 2005) and used in the estimation of minimum Doppler factor. The data were analyzed using XRT data analysis software (XRTDAS) distributed within the HEASOFT package (v6.19). The cleaned event files were generated using *xrtpipeline-0.13.2* tool, and *xrtproduct-0.4.2* tool was used to generate spectral files. The spectra observed during flares p1 and p4 (marked in Figure 1) were added using an *addspec* tool and rebinned with a minimum of 20 photons per bin. The final spectrum was then fitted with an absorbed power-law model with a neutral hydrogen column density,  $n_H$  fixed at the galactic value of  $1.81 \times 10^{20}$   $\text{cm}^{-2}$  (Kalberla et al. 2005).

<sup>2</sup> <https://heasarc.gsfc.nasa.gov/docs/archive.html>

### 2.3. *Optical observations from SPOL*

The spectroscopic data<sup>3</sup> from SPOL CCD Imaging/Spectropolarimeter at Steward observatory at the University of Arizona were used in this work. It combines polarizing optics and a transmission-optics spectrograph into a self-contained, portable, and high-throughput instrument. The complete details and explanation of the data is given in [Smith et al. \(2009\)](#). The SPOL regularly monitors Ton 599 as a part of the *Fermi* multiwavelength support program. The V-band magnitude and the linear polarization data since 2011 were obtained from SPOL.

### 2.4. *Optical-UV observations from Swift-UVOT*

The optical-UV data<sup>4</sup> from *Swift*-UVOT ([Roming et al. 2005](#)) were also analyzed and used to estimate the magnetic field in the emission region. The optical data are provided in three filters, viz. *V*, *B* and *U*, while the data in UV bands are available in *UVW1*, *UVM2* and *UVW2* filters. The observed magnitudes were corrected for a galactic extinction of  $E_{B-V} = 0.0171$  mag ([Schlafly & Finkbeiner 2011](#)). The corrected observed magnitudes at all six wavelengths were then converted into the flux using zero point magnitudes ([Poole et al. 2008](#)).

### 2.5. *Radio observations from OVRO*

Ton 599 is also regularly monitored in radio by 40 m Owens Valley Radio Observatory (OVRO) as a part of *Fermi* monitoring program, since 2008 January 1 (MJD 54473). The complete details of the observing program and calibration are given in [Richards et al. \(2011\)](#) and [Richards \(2012\)](#). The off-axis dual-beam optics and a cryogenic receiver with 3 GHz bandwidth centered at 15 GHz are used in the telescope. The total flux density measurements are performed using 'double-switching' procedure. This method removes receiver gain fluctuations, ground and atmospheric pick-up effects. The typical uncertainty in total flux density measurement is about 3 mJy. This uncertainty includes the contribution from total system temperature ( $\sim 55$  K at zenith), atmospheric and cosmic microwave background temperature. Besides the measured error, the 2 % error comes from residual pointing.

<sup>3</sup> <http://james.as.arizona.edu/~psmith/Fermi/>

<sup>4</sup> <https://heasarc.gsfc.nasa.gov/docs/archive.html>



These two errors are added in quadrature for each measurement. All the data<sup>5</sup>, since 2008 January 1, till 2018 April 4 (MJD 58212) are used in this work.

### 3. RESULTS

We have extensively studied the long-term lightcurve in  $\gamma$ -ray band (0.1 - 300 GeV) and identified four periods during which the source was in high flux state. The flares were selected based on flux exceeding  $5.5 \times 10^{-7} \text{ph cm}^{-2} \text{s}^{-1}$ . This flux corresponds to  $3 \sigma$  value of the mean background flux of  $2.36 \times 10^{-7} \text{ph cm}^{-2} \text{s}^{-1}$ . The periods around the peak flux were chosen arbitrarily for detailed study. The detailed activity of the source in these four periods is discussed in this section.

#### 3.1. Long-term lightcurve

The Figure 1 shows ten days binned *Fermi*-LAT lightcurve encompassing four high flux states marked by p1, p2, p3, and p4. It can be seen that the first high flux state (p1) was observed on MJD  $55435 \pm 5$  with the flux of  $(8.3 \pm 0.4) \times 10^{-7} \text{ph cm}^{-2} \text{s}^{-1}$ . After that the source went into the quiescent state for almost five years with average flux level of  $\sim 10^{-7} \text{ph cm}^{-2} \text{s}^{-1}$ . Towards the end of 2015 i.e on MJD  $57345 \pm 5$ , it again went into the flaring state (p2) during which the observed flux was  $(5.9 \pm 0.4) \times 10^{-7} \text{ph cm}^{-2} \text{s}^{-1}$ , which is  $\sim 40\%$  lower than p1. The third flare (p3) was observed almost after one and half year in the middle of the year 2017 (MJD  $57955 \pm 5$ ). The peak flux during p3,  $(7.62 \pm 0.54) \times 10^{-7} \text{ph cm}^{-2} \text{s}^{-1}$ , was comparable to that of p1. Recently the source had again gone into the high flux state (p4) of  $(14.5 \pm 0.6) \times 10^{-7} \text{ph cm}^{-2} \text{s}^{-1}$ , which is the highest ever detected flux in *Fermi*-LAT era for this source. We have studied these four flares in detail by scanning these periods on shorter timescale of one day except for p2, where the binning of two days is used, due to sparse sampling. Through detailed observations we found several sub-flares during major flares, p1, p2, p3, and p4, which is discussed in this section along with the flare fitting method. The change of polarization in optical band during p4 is also discussed in this section. Due to sparse sampling of the polarization data during p1, p2, and p3, it is not studied for these periods.

<sup>5</sup> [http://www.astro.caltech.edu/ovroblazars/data.php?page=data\\_query](http://www.astro.caltech.edu/ovroblazars/data.php?page=data_query)

### 3.1.1. Flare fitting

In order to understand the flaring pattern within the major flare, we fit each individual component and a constant baseline flux in the whole one/two-day binned lightcurve. This decomposition of the flare is relatively simple but potentially very useful way of understanding the flux variations in the various energy bands (Valtaoja et al. 1999). This method is also very useful in probing the shorter timescale (of the order of minutes) variability seen at  $\gamma$ -ray energies. The time dependent profile used for each component is,

$$F(t) = 2F_0(\exp^{(t_0-t)/T_r} + \exp^{(t-t_0)/T_d})^{-1}, \quad (5)$$

where,  $F(t)$  is the flux at time  $t$ ,  $t_0$  is the sub-flare peak time,  $T_r$  and  $T_d$  are the rise and fall time respectively and  $F_0$  is the flux at time  $t_0$ , which represents the amplitude of the sub-flare.

We first fitted each individual sub-flaring component with the function given in Equation 5 and obtained the function parameters. Then the final best-fit is obtained for the total function consisting of  $n$  such sub-flaring components and one constant background component. We use the fit parameters of individual sub-flares as the starting parameters while performing the fit of the total function for a given period. The residual of the fit which is the ratio of the difference of the model and observed flux to the flux-error ((Model flux - observed flux)/flux error) is given in the second panel of Figures 2, 3, 4 and 5, to validate the combined fit of each period. Similar method was used in the analysis of temporal structure of the ten bright blazars in the work by Abdo et al. (2010b). For 3C 454.3, it was also used in studying an exceptional event of 5 day  $\gamma$ -ray outburst occurred in 2010 November (Abdo et al. 2011) and for outbursts observed in 2009 December and 2010 April (Ackermann et al. 2010).

We also note that in the combined fit, some data points lie above the model fit and they seem to be sub-flaring components but we did not model such components as long as its residuals are within  $3\sigma$ . This could be due to superposition of small amplitude flare over ongoing large amplitude but slowly rising/decaying flare.

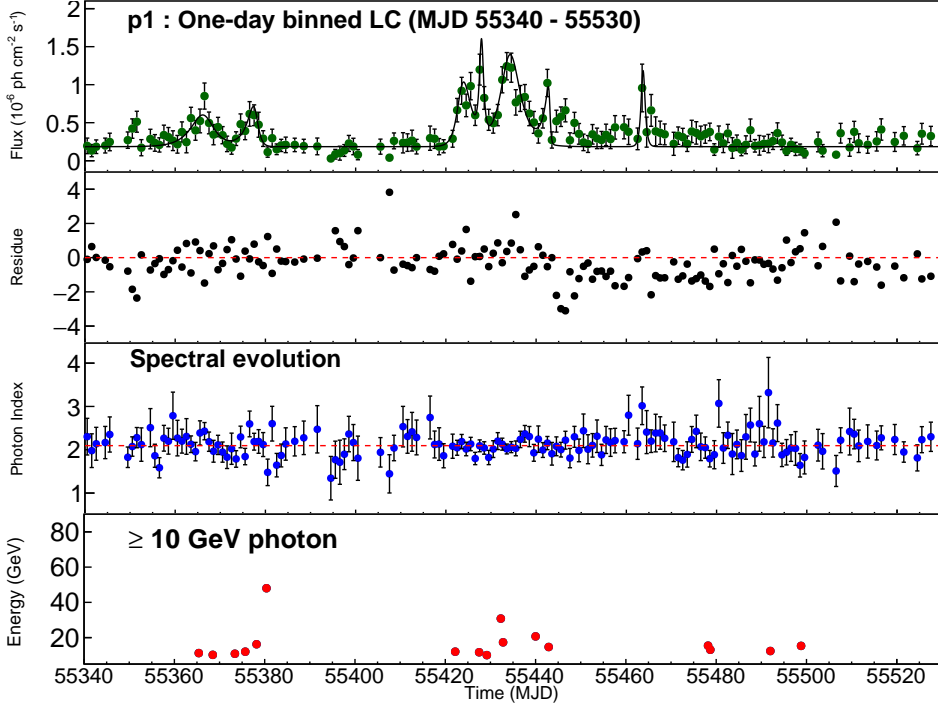


**Figure 2.** *Panel-1:* Lightcurve fitted with seven flaring components and constant background component,  $\chi^2/ndf = 1.47$ ; *Panel-2:* Residual of model fit; *Panel-3:* Power-law index variation during the flare-p1, red dashed line corresponds to the value of spectral index given in 3FGL catalog for Ton 599; *Panel-4:* Photons with energy  $\geq 10$  GeV associated with the source with probability  $\geq 0.99$ .

### 3.1.2. Flare p1

For a detailed study of the flare p1, we generated the one day binned lightcurve for the period MJD 55340-55530, as shown in the first panel of Figure- 2. In this period we identified seven sub-flares, which were fitted using the temporal profile as per the Equation 5 and the constant baseline flux. The parameters of the fit are mentioned in Table 1. During this flare there was no significant change in the spectral shape, as can be seen in the third panel of Figure 2. The highest energy (HE) photon detected during this period had the energy of 48.02 GeV. It was detected on MJD 57380, when the second component of the major flare was decaying.

### 3.1.3. Flare p2

To understand the sub-structure in the flare p2, we made the two-day binned lightcurve for MJD 57250-57500. We observe five sub-flares during this period. The combined fit was obtained by fitting

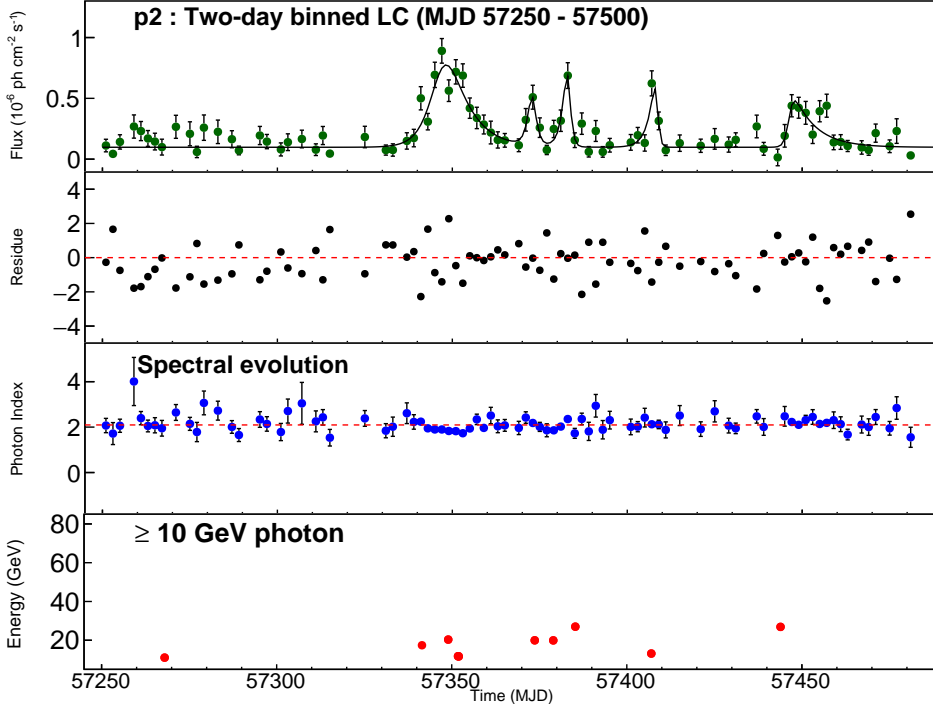


**Figure 3.** *Panel-1:* Lightcurve fitted with five flaring components and constant background component,  $\chi^2/ndf = 1.50$ ; *Panel-2:* Residual of model fit; *Panel-3:* Power-law index variation during the flare-p2, red dashed line corresponds to the value of spectral index given in 3FGL catalog for Ton 599; *Panel-4:* Photons with energy  $\geq 10$  GeV associated with the source with probability  $\geq 0.99$ .

five components to these sub-flares and one constant background component (see Figure 3). The fit parameters are given in Table- 1. During this period also spectrum was almost flat and the highest photon energy of 27.02 GeV was detected during this period.

#### 3.1.4. Flare p3

One-day binned lightcurve for MJD 57920-57990 was generated to analyze the flare-p3. During p3 one long duration sub-flare was resolved. This lightcurve was fitted with one flaring component and one constant background component. The fit is shown in Figure-4 and corresponding fit parameters are mentioned in Table 1. The flat spectral evolution was consistent with p1 and p2, which can be seen in Figure- 4. Only few HE photons were detected during p3, with the highest one of energy 28.9 GeV on MJD 57957.

#### 3.1.5. Flare p4

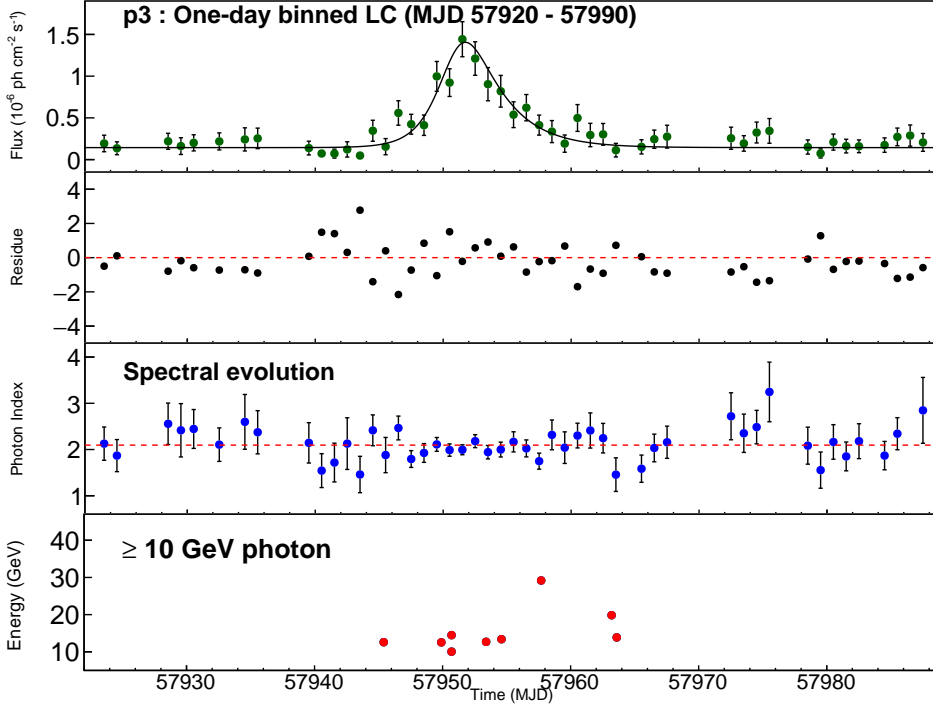


**Figure 4.** *Panel-1:* Lightcurve fitted with one flaring component and constant background component,  $\chi^2/ndf = 1.00$ ; *Panel-2:* Residual of model fit; *Panel-3:* Power-law index variation during the flare-p3, red dashed line corresponds to the value of spectral index given in 3FGL catalog for Ton 599; *Panel-4:* Photons with energy  $\geq 10$  GeV associated with the source with probability  $\geq 0.99$ .

The peculiar flare p4 is the brightest among the four flares observed in  $\gamma$ -ray band. This flare was studied by binning the lightcurve for MJD 58020 - 58120 in one day bin. Six sub-flares were found during this flare and fitted with six flaring components plus one background component. The combined fit is shown in Figure 5. The parameters of this combined fit are mentioned in Table 1. The third panel in Figure 5 shows the variation of the spectral index during p4, which is consistently harder than previous three flares. Also this flare was different in a sense that the bunch of HE photons were detected during this period, with the highest photon energy of 76.94 GeV on MJD 58059.

The variation in the degree of polarization and the angle of polarization was also seen in optical band during flare-p4. These variations are shown in panel-5 and panel-6 of Figure 5, respectively. The degree of polarization was found to increase from  $(4.35 \pm 0.05)\%$  to  $(22.3 \pm 0.1)\%$  and again decrease to  $(6.72 \pm 0.06)\%$  in period of 8 days from MJD 58072 to 58079. Similar variation was seen

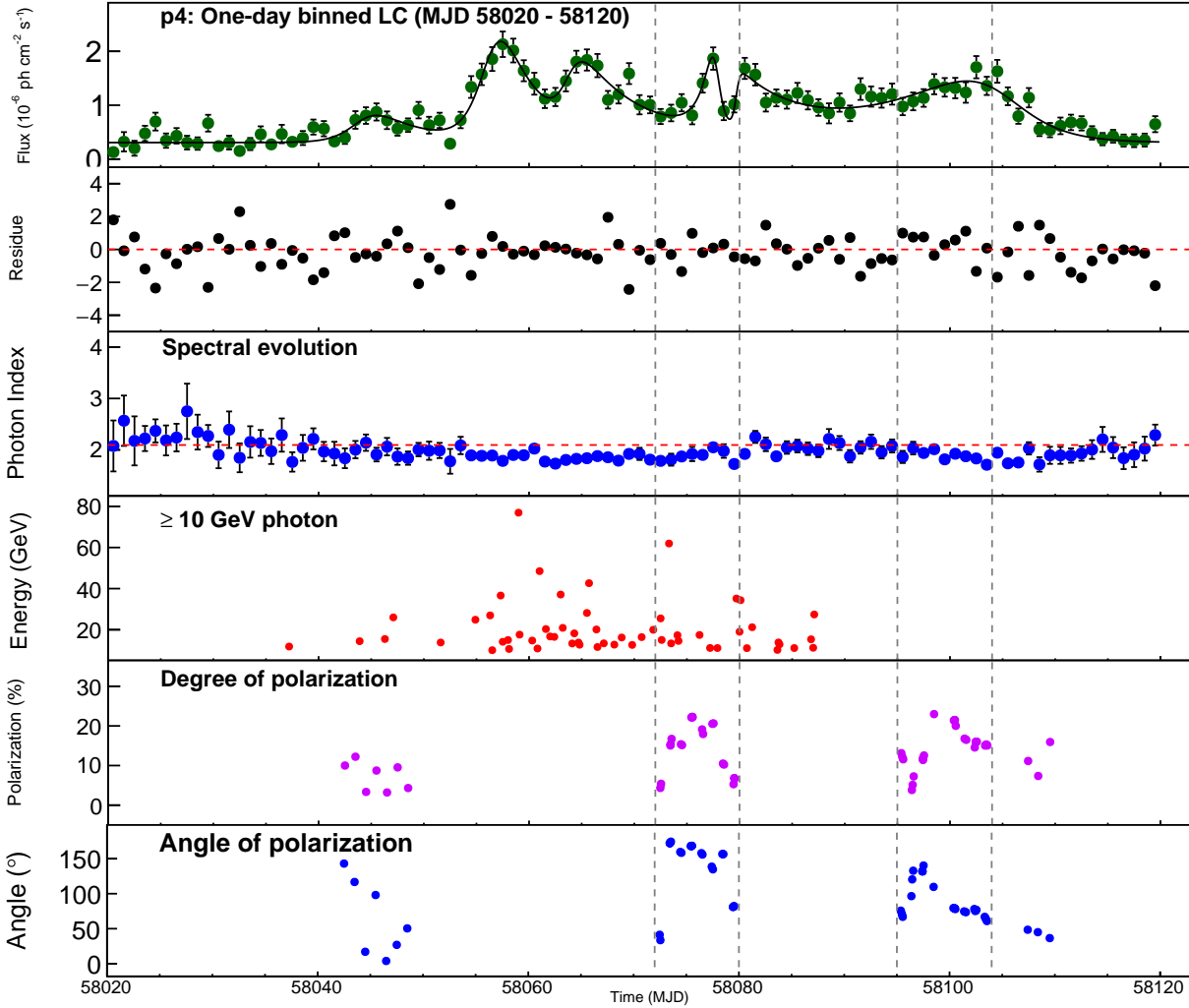


**Figure 5.** *Panel-1:* Lightcurve fitted with six flaring components and a constant background component,  $\chi^2/ndf = 1.32$ ; *Panel-2:* Residual of model fit; *Panel-3:* Power-law index variation during the flare-p4, red dashed line corresponds to the value of spectral index given in 3FGL catalog for Ton 599; *Panel-4:* Photons with energy  $\geq 10$  GeV associated with the source with probability  $\geq 0.99$ . *Panel-5:* The degree of polarization in percentage and *Panel-6:* The angle of polarization in degrees from SPOL data. The periods during which change in degree of polarization of  $\gtrsim 70$  % was observed are shown by dotted gray lines.

during the next observation season, where it was observed to increase from  $(3.83 \pm 0.1)\%$  to  $(22.98 \pm 0.17)\%$  and again decrease to  $(7.37 \pm 0.04)\%$  in period MJD 58096-58108. These periods are shown by dashed lines in last two panels of Figure 5. In relatively low flux state, the degree of polarization was seen to be almost constant. [Wills et al. \(1983\)](#) observed the high degree of linear polarization of 28.05 %, for this source, on 1981 January 31. The model proposed by [Marscher et al. \(2008\)](#)

suggests that the optical polarization can increase substantially during first flare when a disturbance passes through acceleration and collimation zone. However, this does not happen for the second flare during which radio emissions take place and the disturbance crosses a standing shock region. The comparison of radio and optical polarization data would be useful in better understanding the  $\gamma$ -ray flares. Due to sparse sampling of optical polarization data in our case, we could not relate radio and optical polarization data.

### 3.1.6. Doubling/halving time

The flux doubling/halving timescale analysis was done with the data points of entire period of four shorter timescale lightcurves, independent of flare fitting method. This analysis was carried out to acquire the confidence on rise and decay times that are obtained from the flare fitting method. We scanned all four shorter timescale lightcurves for the fastest flux doubling/halving time using following equation,

$$F(t_2) = F(t_1)2^{(t_2-t_1)/\tau_d}, \quad (6)$$

where  $F(t_1)$  and  $F(t_2)$  are the fluxes at time  $t_1$  and  $t_2$ , respectively, and  $\tau_d$  is the flux doubling/halving timescale. The doubling/halving timescale from consecutive time instances, having significance above  $3 \sigma$  are listed in the Table 2. The fastest doubling/halving timescales obtained using this method during four flares are 0.37, 0.89, 0.35 and 0.75 days with the significance of  $5.82 \sigma$ ,  $7.29 \sigma$ ,  $7.64 \sigma$ , and  $4.03 \sigma$ , respectively. We have checked doubling/halving time for its coincidence with sub-flaring components and it is mentioned in the first column of Table 6. It is seen that the most of the sub-flaring components during all four flares coincide with the significant doubling/halving time. Also, the flux doubling/halving timescales are consistent with the corresponding rise/decay times obtained from the flare fitting method.

### 3.2. Variation of Mg-II line

To study the spectroscopic behavior of Ton 599, optical spectra were obtained from SPOL observatory. These spectra show the prominent Mg-II line at wavelength of  $2800 \text{ \AA}$ , which is red-shifted to  $4830 \text{ \AA}$  for Ton 599. One of the spectra for Ton 599 from SPOL observations is shown in Figure 6.

**Table 1.** Parameters of components identified during flare-p1,p2,p3 and p4 as shown in Figure 2, 3, 4 and 5, respectively

Sub flare	$t_0$	$F_0$	$T_r$	$T_d$
	MJD	$10^{-7}\text{ph}^{-1} \text{ cm}^{-2} \text{ s}^{-1}$	day	day
p1-c1	55366.7±1.0	4.13± 0.84	2.54 ± 1.08	1.97 ±0.88
p1-c2	55377.8±1.2	4.67± 1.46	1.71±0.81	0.61±0.31
p1-c3	55423.4±0.5	0.80± 0.00	0.95±0.32	1.86±0.42
p1-c4	55427.9±0.2	12.00±0.00	0.40±0.19	0.40±0.15
p1-c5	55434.1±0.4	12.00±0.00	1.74±0.31	2.11±0.39
p1-c6	55443.0±0.3	5.45±1.41	1.22±0.55	<b>0.17±0.14</b>
p1-c7	55463.7±0.6	10.00±0.00	0.40±0.28	0.40±0.40
p2-c1	57346.8±1.51	6.42± 0.64	3.11±0.90	6.09±1.23
p2-c2	57372.8±1.95	4.00± 0.00	1.11±0.94	0.98±0.75
p2-c3	57383.1±0.95	5.64± 1.72	1.34±0.72	0.67±0.39
p2-c4	57408.4±0.59	4.00± 0.00	1.96±0.61	0.49±0.39
p2-c5	57446.4±0.78	2.66± 0.56	0.73±0.41	6.45±1.60
p3-c1	57951.1±0.4	12.00± 0.00	1.45±0.25	2.78±0.37
p4-c1	58044.2±0.79	4.30 ± 0.66	1.38 ± 0.80	4.47±1.00
p4-c2	58056.4±0.25	16.23±1.07	1.23±0.16	3.37±0.36
p4-c3	58063.8±0.43	8.74±0.96	0.82±0.44	6.06±0.61
p4-c4	58077.8±0.21	11.52±1.43	1.11±0.29	<b>0.42±0.13</b>
p4-c5	58079.7±0.22	5.80±0.91	0.21±0.12	5.76±0.77
p4-c6	58104.4±0.70	9.62±0.57	9.51±0.84	2.99±0.49

NOTE—A constant baseline flux values of  $(1.85 \pm 0.08) \times 10^{-7}$ ,  $(9.78 \pm 0.87) \times 10^{-8}$ ,  $(1.44 \pm 0.15) \times 10^{-7}$  and  $(3.07 \pm 0.19) \times 10^{-7} \text{ ph cm}^{-2} \text{ s}^{-1}$  for flare-p1,p2,p3 and p4, respectively were also fitted to the data along with sub-flaring components. The decay times shown in boldface were used in calculation of minimum Doppler factor.



**Table 2.** Doubling/halving timescales for lightcurves shown in Figures 2, 3, 4 and 5

Flare	$t_1$	$t_2$	Flux-1	Flux-2	Doubling/halving time	significance	Rise/decay
	(MJD)	(MJD)	( $10^{-7}$ ph cm $^{-2}$ s $^{-1}$ )	( $10^{-7}$ ph cm $^{-2}$ s $^{-1}$ )	(day)	( $\sigma$ )	(R/D)
	55407.5	55408.5	0.39±0.38	2.61±1.04	0.37	5.82	R
p1-c3	55421.5	55422.5	2.88±1.11	6.65±1.54	0.83	3.40	R
p1-c4	55426.5	55427.5	5.98±1.34	11.98±2.03	0.99	4.46	R
p1-c5	55431.5	55432.5	5.99±1.39	10.64±1.72	1.21	3.32	R
p1-c6	55441.5	55442.5	5.58±1.28	10.22±1.80	1.44	3.63	R
p1-c6	55442.5	55443.5	10.22±1.80	2.73±1.07	0.52	4.17	D
p1-c7	55462.5	55463.5	2.87±1.43	9.57±3.14	0.58	4.69	R
	55506.5	55507.5	0.79±0.51	3.62±1.30	0.46	5.53	R
	57277.0	57279.0	0.59±0.47	2.59±1.04	0.94	4.28	R
	57339.0	57341.0	1.73±0.72	5.00±0.95	1.31	4.55	R
	57343.0	57345.0	3.08±0.68	6.93±1.04	1.71	5.68	R
p2-c1	57347.0	57349.0	8.90±1.01	5.63±0.89	3.02	3.23	D
p2-c2	57369.0	57371.0	1.14±0.53	3.23±0.93	1.33	4.00	R
p2-c3	57377.0	57379.0	0.75±0.38	2.48±0.71	1.16	4.54	R
p2-c3	57381.0	57383.0	3.16±0.88	6.87±1.06	1.79	4.21	R
p2-c4	57383.0	57385.0	6.87±1.06	1.56±0.61	0.94	5.01	D
p2-c4	57389.0	57391.0	0.61±0.43	2.32±0.86	1.03	3.98	R
	57405.0	57407.0	1.33±0.67	6.23±1.03	0.89	7.29	R
	57409.0	57411.0	3.15±0.73	0.73±0.43	0.95	3.31	D
	57457.0	57459.0	4.39±0.95	1.38±0.60	1.20	3.19	D
	57469.0	57471.0	0.75±0.43	2.14±0.75	1.32	3.25	R
	57943.5	57944.5	0.48±0.39	3.45±1.25	0.35	7.64	R
	57945.5	57946.5	1.54±0.96	5.58±1.46	0.54	4.16	R
	57948.5	57949.5	4.12±1.22	9.97±1.78	0.78	4.79	R
p3-c1	57950.5	57951.5	9.22±1.65	14.46±2.10	1.55	3.13	R
	58028.5	58029.5	2.89±1.15	6.67±1.56	0.83	3.28	R
	58051.5	58052.5	7.18±1.42	2.87±1.09	0.75	3.03	D
	58052.5	58053.5	2.87±1.09	7.26±1.52	0.75	4.03	R
p4-c2	58053.5	58054.5	7.26±1.52	13.38±2.02	1.13	4.02	R
	58075.5	58076.5	8.10±1.65	14.09±1.78	1.25	3.63	R
p4-c4	58077.5	58078.5	18.65±2.07	8.93±1.70	0.94	4.69	D
p4-c5	58079.5	58080.5	10.17±1.5	16.83±1.97	1.38	4.40	R
	58090.5	58091.5	8.49±1.47	13.00±2.01	1.63	3.10	R
p4-c6	58107.5	58108.5	11.40±1.79	5.50±1.22	0.95	3.29	D

NOTE—The doubling/halving time is in observed frame.

For this source we have obtained 140 spectra during the period of 2011 to 2018, to study the variation of the Mg-II line parameters.

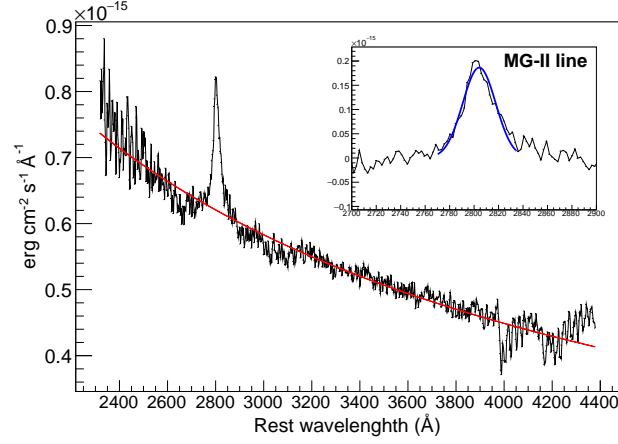


**Figure 6.** An optical spectrum from SPOL with continuum fitted with a power-law which is shown by red curve; Inset : A Gaussian fit to the Mg-II line after subtracting the power law continuum.

The Mg-II line profile is fitted with the Gaussian function after subtracting the underlying power law continuum which is shown in the inset of Figure 6. The Figure 7 shows the variation of the equivalent width (EW) of the Mg-II line with continuum. It can be seen that the EW is inversely proportional to the underlying continuum, which suggests that the variations of the Mg-II line are less than that of the continuum. It was seen that absolute flux of Mg-II line was more or less constant

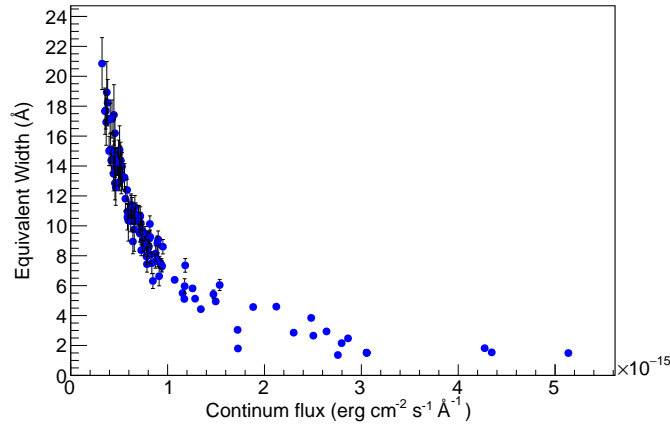


**Figure 7.** The variation of the equivalent width of the Mg-II line with continuum flux

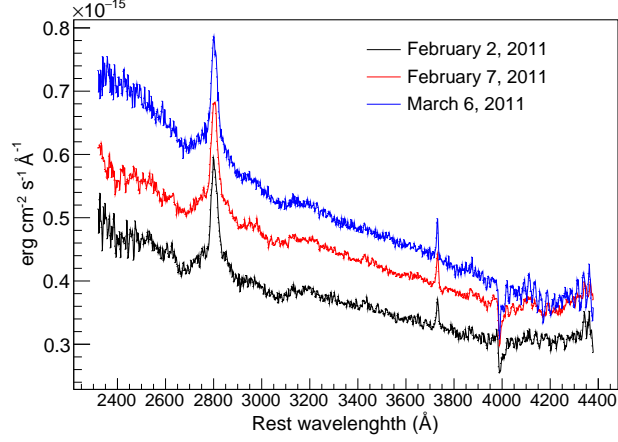


**Figure 8.** SPOL spectra that exhibited the O-II line along with the Mg-II line.

with the changes in continuum flux, which also means that variations in Mg-II line are uncorrelated with the variations in continuum flux. It is also seen that during high continuum flux state the Mg-II line is not visible in the optical spectra. It is possible that the line is concealed in the continuum during the high flux state. This might be due to little or no effect of different levels of the flux state on BLR, from where the Mg-II line is thought to be originating. For Ton 599, the optical spectra were studied to see the effect of an ionizing continuum on the Mg-II line in 1981 by [Wills et al. \(1983\)](#). They reported that the optical spectrum is featureless like BL Lac when the source is bright and in the faint state the spectrum appeared to be that of normal quasi stellar object (QSO). Similar results were seen for other blazars CTA 102 ([Larionov et al. 2016](#)), 3C 454.4 ([Raiteri et al. 2008](#)) and OJ 248 ([Carnerero et al. 2015](#)). These suggest that enhanced  $\gamma$ -ray activity of the jet may have little or no effect on BLR.

It was observed that, apart from the Mg-II line, some of the optical spectra also exhibited a narrow O-II line at the restframe wavelength of 3725 Å. These spectra are shown in Figure 8. As this line is seen in very few spectra, we did not study the variations of this line in detail.

### 3.3. *The correlation between $\gamma$ -ray and radio band*

The correlation between  $\gamma$ -ray and radio emission is quantified by using a discrete correlation function (DCF) given by [Edelson & Krolik \(1988\)](#). We use this function on the discrete data set

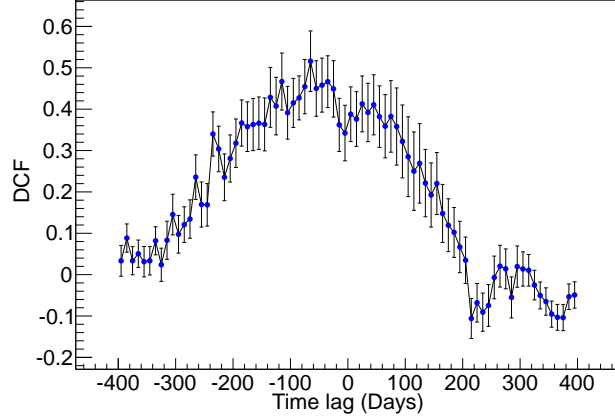


**Figure 9.** DCF between radio and  $\gamma$ -ray band. Here negative time-lag means that radio emission lags behind the  $\gamma$ -ray emission.

of  $\gamma$ -ray and radio band, spanning almost nine years period. These data sets are linearly detrended (Welsh 1999) before estimating DCF. For all measured pairs  $(a_i, b_i)$  having pairwise lag  $\Delta t_{ij} = t_j - t_i$ , unbinned discrete correlation function is defined as,

$$UDCF_{ij} = \frac{(a_i - \bar{a})(b_j - \bar{b})}{\sqrt{(\sigma_a^2 - e_a^2)(\sigma_b^2 - e_b^2)}}, \quad (7)$$

DCF is then given by averaging M pairs for which  $(\tau - \Delta\tau/2) \leq \Delta t_{ij} < (\tau + \Delta\tau/2)$ ,

$$DCF(\tau) = \frac{1}{M}UDCF_{ij}, \quad (8)$$

The error on DCF is given by,

$$\sigma_{DCF}(\tau) = \frac{1}{M-1} \left\{ \sum [UDCF_{ij} - DCF(\tau)] \right\}^{1/2}, \quad (9)$$

A correlation coefficient of  $0.52 \pm 0.07$  is seen between the radio and  $\gamma$ -ray band with radio emission lagging behind the  $\gamma$ -ray emission by  $(65 \pm 10)$  days. Similar time-lag was also reported by Max-Moerbeck et al. (2014). This suggests that  $\gamma$ -ray emission originates upstream of radio emissions. We also checked the DCF by excluding the initial three years of radio and  $\gamma$ -ray data (upto MJD 56000), during which the double-peak behavior is observed in radio band. It is found that the lag of  $(65 \pm 10)$  days is largely coming from this period. Excluding the data upto MJD 56000, gave slightly less significant peak at 85.0 day with correlation coefficient of  $0.55 \pm 0.17$ . Such double-peak

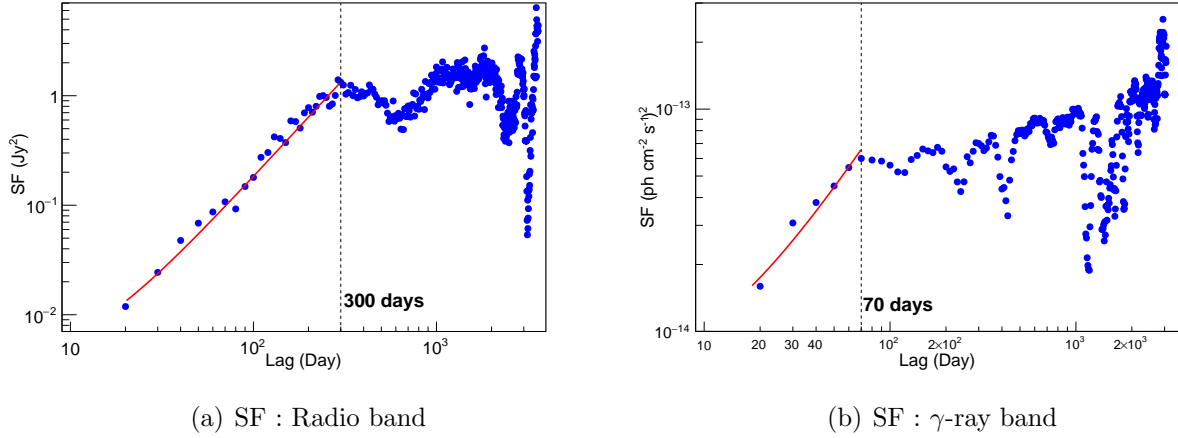
structure during this period was also seen at 37 GHz (13.7 m telescope at Aalto University Metsähovi Radio Observatory, Finland ), 43 GHz (VLBA data) and 230 GHz (1.3mm, the Submillimeter Array (SMA)) and the results from these observations are reported by [Ramakrishnan et al. \(2014\)](#). For this source, the radio emission was lagging the  $\gamma$ -ray emission by 81.55 days, in the cross correlation study carried out between 37 GHz Metsähovi lightcurves and the *Fermi*-LAT  $\gamma$ -ray lightcurve by ([León-Tavares et al. 2011](#)), for the data spanning the period of 2007-2010.

### 3.4. The structure function (SF)

To study the characteristic timescales in the lightcurve, DCF, Lomb-Scargle periodogram and structure function methods are generally used in the time series analysis. The periodic variation in radio band can be seen in the second panel of Figure 1. To look for any periodicity in this band and also in  $\gamma$ -ray band, we used the SF method ([Simonetti et al. 1985](#)). It is used to evaluate the distribution of power in a lightcurve. The SF operates in the time domain and can be used to examine irregularly sampled lightcurves. This analysis is done on almost nine years of radio and  $\gamma$ -ray data. The first order SF is given by,

$$SF(\tau) = \frac{1}{n} \sum_{ij} [S(t_i) - S(t_j)]^2, \quad (10)$$

where,  $S(t_i)$  and  $S(t_j)$  is the flux density at time  $i$  and  $j$  respectively. Here,  $\tau$  is time-lag and  $n$  is number of pairs within the time lag  $|t_i - t_j| \sim \tau$ . If there is a variability above the noise level, the SF rises monotonically with a power law shape and reaches its first maximum at a plateau. The intersection of the power-law fit with the plateau defines the characteristic timescale ( $\tau_c$ ) which is an indication of the nature of the process of flux variation ([Hughes et al. 1992](#)). The SF of Ton 599 at 15 GHz is plotted in Figure 10(a). From the SF analysis of nine years of radio data, we find a slope of fitted power-law to be 1.82 and period of  $\sim 300$  days (0.82 year). Similar analysis was done on data collected over  $\sim 33$  years from 1980 January to 2012 June by [Liu & Liu \(2014\)](#). They reported similar  $\tau_c$  of  $1.15 \pm 0.05$  years at three wavelengths of 4.8, 8.0 and 14.5 GHz. The work by [Hovatta et al. \(2007\)](#) on the long-term variability of AGNs, mentioned this timescale to be 1.21 and 1.36 year,



(a) SF : Radio band

(b) SF :  $\gamma$ -ray band

**Figure 10.** The SF for radio and  $\gamma$ -ray band. The characteristic timescale is shown by dashed line in SF plot.

respectively, at 22 and 37 GHz. We note that, at similar radio frequency, the value of  $\tau_c$  obtained in this work differs by  $\sim 28\%$ , with that reported by Liu & Liu (2014).

The SF of  $\gamma$ -ray lightcurve is shown in Figure 10(b). In this band the characteristic timescale and the power-law index was found to be  $\sim 70$  days and 1.30, respectively. Here,  $\tau_c$  in  $\gamma$ -ray band is shorter than that of radio band. This could be an indication of slower nature of the mechanism responsible for flux variation in radio band as compared to  $\gamma$ -ray band. In case,  $\gamma$ -ray and radio flux variation are produced by the same mechanism (cooling could be possible mechanism), then it could be indicative of a decaying nature of such process. Marscher et al. (2008) suggest that at the base of the jet, explosive activity injects the surge of energy into the jet. This disturbance which appears as a knot of emission, propagates through the acceleration and collimation zone. This causes the emission of optical, X-ray and  $\gamma$ -ray radiation from the knot, until it exits the zone. Owing to synchrotron self-absorption, this zone is opaque at radio wavelengths and these are emitted at much downstream of the jet in the standing shock when the second flare takes place (Marscher et al. 2008).

#### 4. TIME-RESOLVED SED

Four major peaks can be clearly seen in the  $\gamma$ -ray lightcurve shown in Figure 1 marked as p1, p2, p3, and p4. It is also seen that the spectral evolution is similar during p1, p2 and p3, however, during

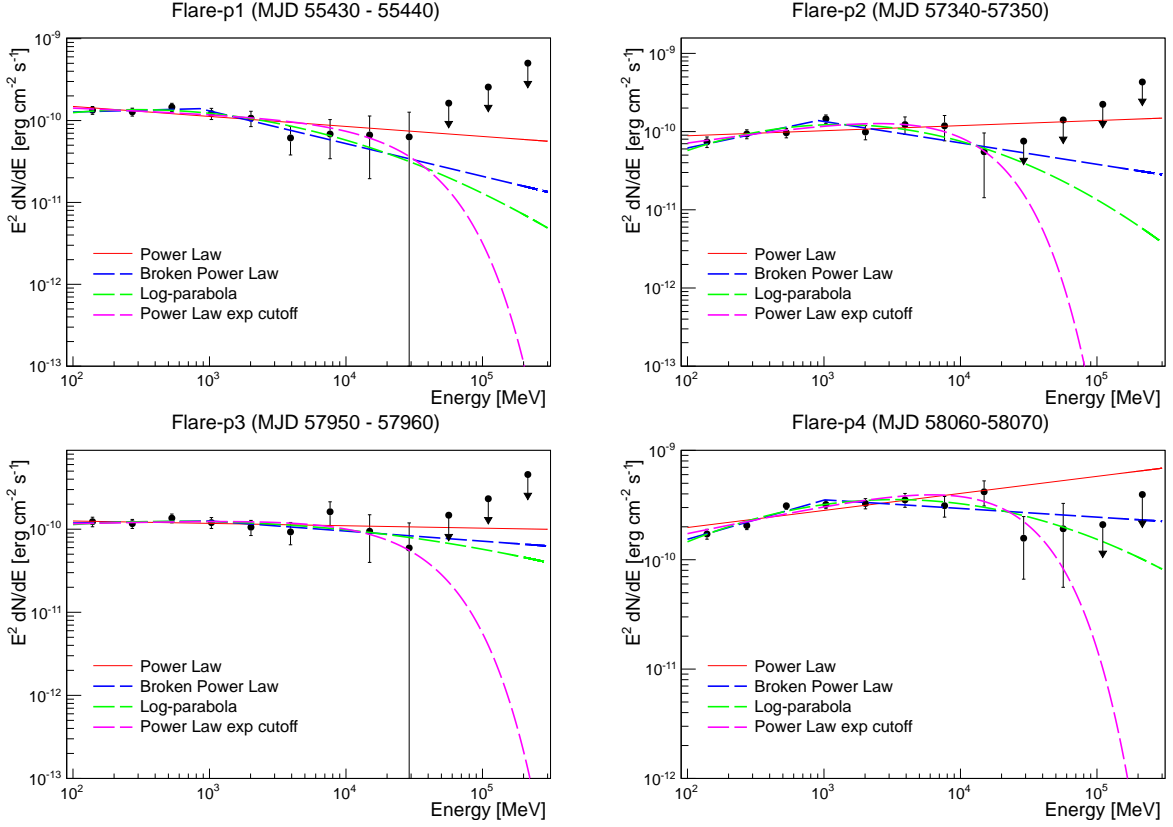


**Figure 11.** The 10-day averaged SED for Ton 599 during four flares p1, p2, p3, and p4, along with best fit PL, BPL, LP and PLEC functions

p4 it is consistently harder. In this section, we focus on the spectral studies of these four peaks which are occurring at four different epochs.

In a spectral analysis, SED data points are computed in an equally spaced logarithmic bins in the energy range of 0.1-300 GeV. Four spectral models used in the likelihood fit for Ton 599 are defined in Equation 1- 4, mentioned in Section 2 (respectively as PL, BPL, LP and PLEC). The best-fit parameters of the models are mentioned in Table 3. The fitted models are plotted in Figure 11 along with SED data points. The value of log-likelihood ratio test is mentioned in Table 3 to check for the improvement of model fit as compared to power-law model. It can be seen that BPL shows significant improvement in the fit, compared to PL, at  $3\sigma$  level for flare p2 and p4, while LP shows improvement in the fit only for p4. For other two flares neither BPL, LP nor PLEC give significant improved fit as compared to PL. We note that, during p4,  $\sim 70\%$  times the spectral index was harder

than that mentioned in *Fermi*-LAT 3FGL catalog (see *Panel-3* of Figure 5), indicating significant hardening of the spectrum.

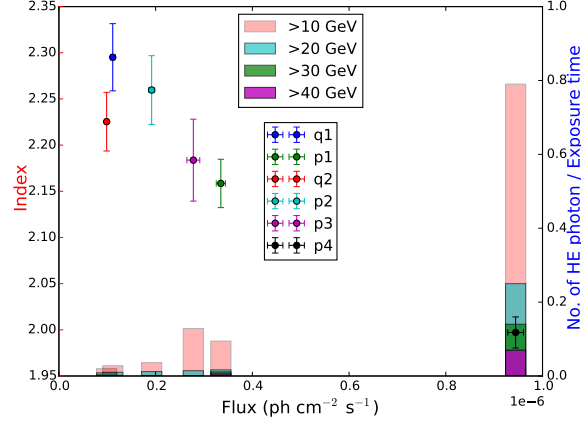


**Figure 12.** A power-law index vs. 0.1-300 GeV flux during six epochs of the source and corresponding rate of emission of HE photons

The Figure 12 shows the correlation between the flux and power-law index during four flaring periods and two quiescent states of the source (see Figure 1). The flux and index are averaged over corresponding periods. The behavior of hardening of the spectra with the flux can be seen in this figure. Also, histograms of high energy photons over total exposure periods of corresponding epochs are shown in Figure 12. It is seen that during peculiar flare p4, the rate of emission of high energy photons has increased, as compared to the previous flares and quiescent states.

## 5. DISCUSSIONS

The various jet parameters like Doppler factor, jet opening angle, magnetic field in the emission region, size and distance of emission region from central black hole are estimated for flare p1 and p4 and discussed in this section. For other two flares, p2 and p3, due to lack of X-ray data, we have not calculated jet parameters during these two periods.

### 5.1. The constraint on Doppler factor

The minimum Doppler factor can be estimated numerically, by  $\gamma\gamma$  opacity argument and from a detection of the highest energy photons during the flare (Dondi & Ghisellini 1995; Ackermann et al.



**Table 3.** Best fit parameters for PL, BPL, LP and PLEC function, obtained from likelihood analysis of spectra during four flares p1, p2, p3, and p4.

Flare	Period	Flux	Luminosity	$\Gamma$		Log(likelihood)	LRT( $\chi^2_{\nu,0.001}$ )
PL	MJD	$10^{-7}\text{ph cm}^{-2}\text{s}^{-1}$	$10^{48}\text{erg s}^{-1}$				
p1	55430-55440	$8.28\pm 0.51$	1.57	$2.12\pm 0.05$		-38070.57	-
p2	57340-57350	$5.90\pm 0.38$	1.46	$2.05\pm 0.05$		-38123.22	-
p3	57950-57960	$7.62\pm 0.54$	1.72	$2.03\pm 0.05$		-39210.28	-
p4	58060-58070	$14.54\pm 0.60$	5.58	$1.84\pm 0.03$		-50572.40	-

	Period	Flux	Luminosity	$\Gamma_1$	$\Gamma_2$	Break	Log(likelihood)	
BPL	MJD	$10^{-7}\text{ph cm}^{-2}\text{s}^{-1}$	$10^{48}\text{erg s}^{-1}$			GeV		
p1	55430-55440	$7.98\pm 0.53$	1.37	$1.96\pm 0.13$	$2.40\pm 0.19$	$0.85\pm 0.62$	-38068.93	3.28(6.91)
p2	57340-57350	$5.33\pm 0.87$	1.63	$1.86\pm 0.20$	$2.27\pm 0.17$	$0.91\pm 0.39$	-38119.56	7.32(6.91)
p3	57950-57960	$7.50\pm 0.58$	1.62	$1.98\pm 0.13$	$2.12\pm 0.15$	$1.00\pm 2.19$	-39210.68	-0.80(6.91)
p3	58060-58070	$13.60\pm 0.63$	4.48	$1.64\pm 0.07$	$2.08\pm 0.07$	$1.02\pm 0.28$	-50566.64	11.52(6.91)

	Period	Flux	Luminosity	$\alpha$	$\beta$	Log(likelihood)	
LP	MJD	$10^{-7}\text{ph cm}^{-2}\text{s}^{-1}$	$10^{48}\text{erg s}^{-1}$				
p1	55430-55440	$7.80\pm 0.52$	1.39	$2.05\pm 0.07$	$0.06\pm 0.04$	-38069.71	1.72(10.83)
p2	57340-57350	$5.32\pm 0.45$	1.27	$1.75\pm 0.09$	$0.12\pm 0.04$	-38119.57	7.30(10.83)
p3	57950-57960	$7.43\pm 0.57$	1.63	$1.98\pm 0.07$	$0.03\pm 0.03$	-39209.86	0.84(10.83)
p4	58060-58070	$13.55\pm 0.63$	4.49	$1.71\pm 0.05$	$0.07\pm 0.02$	-50564.44	15.92(10.83)

	Period	Flux	Luminosity	$\Gamma_{PLEC}$	$E_c$	Log(likelihood)	
PLEC	MJD	$10^{-7}\text{ph cm}^{-2}\text{s}^{-1}$	$10^{48}\text{erg s}^{-1}$		GeV		
p1	55430-55440	$8.17\pm 0.52$	1.46	$2.07\pm 0.08$	$30.19\pm 40.38$	-38111.44	-81.74(10.83)
p2	57340-57350	$5.51\pm 0.43$	1.30	$1.74\pm 0.09$	$9.80\pm 4.40$	-38130.33	-14.22(10.83)
p3	57950-57960	$7.42\pm 0.55$	1.59	$1.96\pm 0.07$	$30.28\pm 26.27$	-39205.93	8.70(10.83)
p4	58060-58070	$13.98\pm 0.61$	4.44	$1.74\pm 0.04$	$23.63\pm 8.27$	-50574.64	-4.48(10.83)

NOTE—LRT is the value of log-likelihood ratio test, compared with the power-law model;  $\chi^2_{\nu,0.001}$  is the value of reduced  $\chi^2$  for  $\nu$  degree of freedom corresponding to the probability of 0.001

2010). Assuming that the optical depth,  $\tau_{\gamma\gamma}(E_1)$  of the photon of energy  $E_1$  to  $\gamma\gamma$  interaction is 1, the minimum Doppler factor ( $\delta_{min}$ ) can be calculated as,

$$\delta_{min} = \left[ \frac{\sigma_t d_l^2 (1+z)^2 f_\epsilon E_1}{4t_{var} m_e c^4} \right]^{1/6}, \quad (11)$$

where,  $\sigma_t$  is the Thomson scattering cross section,  $E_1$  is the highest photon energy,  $d_l$  is the luminosity distance which is 4.5 Gpc for Ton 599,  $t_{var}$  is the observed variability timescale and  $f_\epsilon$  is the 0.3-8 keV flux (as mentioned in Section 2.2). We have estimated the Doppler factor, assuming  $t_{var}$  to be

**Table 4.** The calculated jet parameters for flare p1 and p4

Flare	0.3-8 keV flux ( $10^{-12}$ erg $\text{cm}^{-2}$ $\text{s}^{-1}$ )	HE photon (GeV)	$\delta_{min}$	$\beta_{jet}$	$d$ (pc)	$R'$ ( $10^{15}$ cm)	$\theta$ ( $^{\circ}$ )	$f_e^{sy}$ ( $10^{-10}$ erg $\text{cm}^{-2}$ $\text{s}^{-1}$ )	$\epsilon_{sy}$ ( $10^{-6}$ )	$B_e$ (G)
p1	1.32	48.02	10.75	0.9957	0.014	1.94	5.33	0.24	0.081	14.13
p4	7.67	76.94	13.45	0.9972	0.051	5.86	4.25	1.86	0.203	6.92

the fastest variability timescale ( $\ln 2 \times T_d$ ) observed during each flare. Also the size ( $R'$ ) of the  $\gamma$ -ray emission region is calculated from  $\delta_{min}$  and  $t_{var}$  using  $R' \sim c\delta_{min} t_{var}/(1+z)$ . The distance ( $d$ ) of this region from central engine is then estimated, assuming  $\Gamma \sim \delta_{min}$ , as  $d \sim 2 c\Gamma^2 t_{var}/(1+z)$  (Abdo et al. 2011). The estimated value of these jet parameters are given in Table 4. In earlier studies the viewing angle has been estimated to range from  $2^{\circ}$  to  $8^{\circ}$  (Lähteenmäki & Valtaoja 1999; Hong et al. 2004; Hovatta et al. 2009; Ramakrishnan et al. 2014), consistent with the value of  $5^{\circ}.33$  and  $4^{\circ}.25$  (for flare p1 and p4, respectively) found in this work. The Doppler boosting factor of 28.5 was estimated in earlier work (Hovatta et al. 2009), which is also consistent with the lower limit of 10.75 and 13.45 (for flare p1 and p4, respectively), estimated in this work.

### 5.2. Isotropic luminosity

The luminosity of the source was calculated for each of the spectral shapes (PL, BPL, LP and PLEC) at the peak of all four major flares. The integrated apparent isotropic luminosity is given by,

$$L_{\gamma} = 4\pi d_l^2 \int_{E_1}^{E_2} E \frac{dN(E)}{dE} dE, \quad (12)$$

where,  $dN(E)/dE$  is the differential form of spectral model used in the analysis. Here, the integral is taken over 100 MeV to the highest energy photon detected during each flare. The peak luminosity values during four flares are given in the Table 3. It is observed that the peak luminosity is  $\sim 3$  times higher for p4 than other three flares. The black hole mass of Ton 599 is found to be  $(0.79 - 3.47) \times 10^8 M_{\odot}$  (Liu et al. 2006b; Xie et al. 2004) and thus the Eddington luminosity ( $L_{edd}$ ) is estimated to be  $(1.0 - 4.37) \times 10^{46}$  erg  $\text{s}^{-1}$ . Now, in order for intrinsic luminosity, to be less than Eddington luminosity ( $2(1-\cos\theta)L_{\gamma} \leq L_{edd}$ ),  $\theta$  should be in the range of  $5.09-5.65^{\circ}$ , which is consistent with the results numerically estimated from  $\gamma\gamma$  opacity argument.

### 5.3. Magnetic field

One can also estimate the co-moving magnetic field ( $B_e$ ) in the emission region from the synchrotron peak flux ( $f_\epsilon^{sy}$ ) and the synchrotron peak frequency ( $\epsilon_{sy} = h\nu_{sy}/m_e c^2$ ) using the equation given by Böttcher (2007) as,

$$B_e = 9D_1^{-1} \left[ \frac{d_{27}^4 f_{-10}^2 e_B^2}{(1+z)^4 \epsilon_{sy,-6} R_{15}'^6 (p-2)} \right]^{1/7} G, \quad (13)$$

where,  $f_{-10} = f_\epsilon^{sy}/10^{-10}$  erg cm<sup>-2</sup> s<sup>-1</sup>,  $\epsilon_{sy,-6} = \epsilon_{sy}/10^{-6}$ ,  $R_{15}' = R'/10^{15}$  cm,  $e_B$  is the equipartition parameter in the co-moving frame,  $d_{27} = d_l/10^{27}$  cm and  $p$  is the spectral index of underlying electron spectrum.  $D_1 = D/10$ , where  $D$  is the Doppler factor. For a better estimate of synchrotron peak, we fitted the second order polynomial to the lower-energy part of the SED for flare p1 and p4. These fits are shown in Figure 13. The values of  $f_{sy}$  and  $\epsilon_{sy}$  obtained from these fits are mentioned in Table 4. We have adopted an underlying electron spectral index,  $p = 3.4$  (Celotti & Ghisellini 2008) for both the flares. Assuming the equipartition of energy, magnetic field in the emitting region during each flare is estimated, using corresponding estimated values of Doppler factor ( $\delta_{min}$ ),  $R'$ ,  $f_{sy,-10}$  and  $\epsilon_{sy,-6}$ . These are given in the last column of Table 4. The  $B_e$  estimated here is 14.13 G and 6.92 G for p1 and p4, respectively. The magnetic field of few Gauss generally is found by the modeling of FSRQs. For Ton 599, it was found to be 4 G (Ghisellini et al. 2010) and 5 G (Celotti & Ghisellini 2008). This  $B_e$ , of the order of a few Gauss would produce much lower break ( $\gamma_b \sim 137$ ) in an injected particle distribution for the emission region of size  $\sim 10^{15}$  cm, which is obtained in this work. This suggests that radiative losses would be much more stronger in the emitting region. We also observed the X-ray spectrum to be harder ( $\sim 1.7$ ), which can be associated with EC mechanism for FSRQs, because SSC component tends to be softer (Celotti & Ghisellini 2008). Looking at the composition of the jet, Ghisellini et al. (2010) reported that the jets of FSRQs are matter dominated i.e much of the jet power goes into forming large radio lobe structures and it transforms only few per cent of their kinetic energy into radiation.

### 5.4. Size of BLR

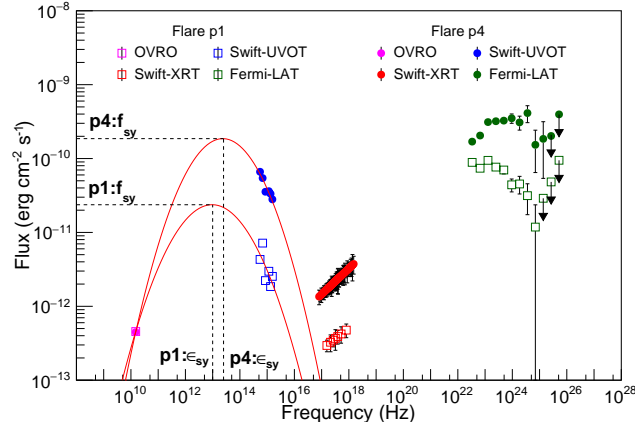


**Figure 13.** SED during p1 and p4, low energy peak fitted with second order polynomial. Here the radio flux is an upperlimit value and it is considered as flux measurement while fitting.

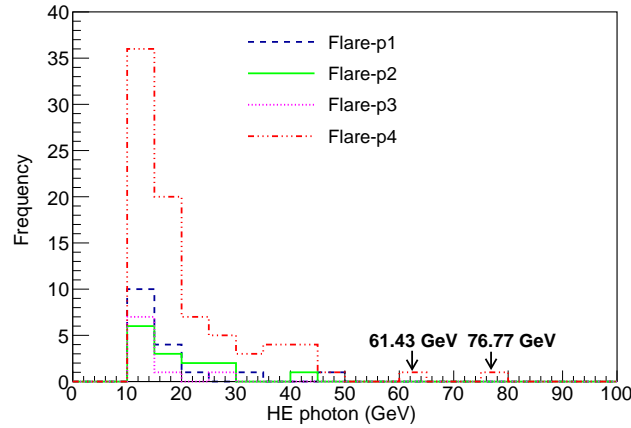


**Figure 14.** The distributions of HE  $\gamma$ -ray photons emitted from the region of  $0.5^\circ$  radius around the source position during flare-p1,p2,p3 and p4.

The BLR is assumed to be a thin spherical shell and its distance from central black hole is given by Ghisellini et al. (2010) as,

$$R_{BLR} = 10^{17} L_{d,45}^{1/2} cm, \quad (14)$$

where,  $R_{BLR}$  is the distance of BLR from the central engine and  $L_{d,45}$  is the accretion disk luminosity in the units of  $10^{45} \text{ erg s}^{-1}$ . Assuming  $L_{BLR}$  to be 10% of  $L_d$ , as this is the fraction of disk luminosity ( $L_d$ ) re-emitted by the broad lines,  $L_d$  is estimated to be in the range of  $(4.47-6.00) \times 10^{45} \text{ erg s}^{-1}$

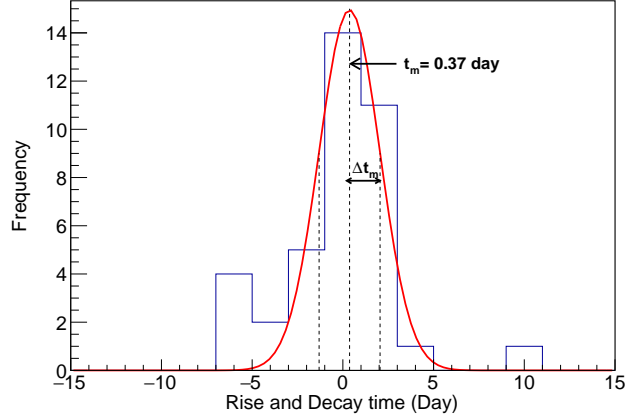


**Figure 15.** The distribution of rise and decay times that are obtained from flare fitting. The positive time corresponds to rise time and negative time corresponds to decay time

(Shaw et al. 2012; Xiong & Zhang 2014; Ghisellini et al. 2010). Hence,  $R_{BLR}$  is estimated to be  $(2.11-2.45) \times 10^{17}$  cm (0.068-0.079 pc).

#### 5.5. Rise and decay time distribution and change in jet parameters over the *Fermi-LAT* era

The excellent sampling of flux measurements in the high energy  $\gamma$ -ray band from *Fermi-LAT* have enabled us to scan the sources in shorter timescales. Figure 15 shows the distribution of all rise and decay times obtained using flare fitting method. It can be seen that the distribution peaks ( $t_m$ ) at 0.37 day with standard deviation ( $\Delta t_m$ ) of 1.68 days. Considering variability time range from  $t_m - \Delta t_m$  to  $t_m + \Delta t_m$ , the Doppler factor varies by  $\sim 33\%$  and  $\sim 23\%$  for flare p1 and p4, respectively.

## 6. CONCLUSION

1. The jet parameters and emission of HE photons: The  $\gamma$ -ray emission region is found to be located between (0.024-0.051) pc from the central engine during flare p1 and p4. The flare-p4 is the highest ever detected flaring state in  $\gamma$ -ray band for this source. We also note that during this period more than 50 photons with the energy above 10 GeV were detected in the span of  $\sim 40$  days. The two highest energy photons, that were observed, had the energies of 76.9 GeV and 61.9 GeV. This is possible if the emission region lies near outer edge or outside the BLR. For emission region to be

near the outer edge of BLR (i.e. 0.08 pc), Doppler factor would have increased upto  $\sim 35$ , during p4, implying the magnetic field of  $\sim 3$  G. The distributions of HE  $\gamma$ -ray photons during four flares are shown in Figure 14. Similar behavior was seen in 3C 454.3 outburst in 2014 May-June with detection of several HE photons above 20 GeV, including one at 45 GeV (Britto et al. 2016).

Alternatively, the phenomenon of emission of bunch of HE photons during flare-p4 for this source, can be explained if the emission region is moving on helical path of the jet (for helical jet models, see, for example, Steffen et al. 1995; Villata & Raiteri 1999; Raiteri et al. 2017). In this case, it is possible that the up-scattered HE  $\gamma$ -ray photons from the emission region may not interact with the BLR clouds as they will not come in the path between the emission region and the observer. The helical jet model proposed by Steffen et al. (1995), was used in the study of 1980-2002 VLBI observations of Ton 599 (Hong et al. 2004). For CTA 102, a helical jet model was used by Shukla et al. (2018) to explain the short-timescale variability on less than the light travel-time across the black hole which is  $\sim 70$  minutes.

2. The  $\gamma$ -ray and radio emission connection : The  $\gamma$ -ray and radio emissions are closely correlated due to the fact that the emission in both these bands are beamed and that both the emissions are produced co-spatially in the jet (for example, León-Tavares et al. 2011; Richards et al. 2014; Fan et al. 2016). The decomposition of the major flare reveals several asymmetric sub-flaring structures in the  $\gamma$ -ray lightcurves. This might be due to an ejection of new particles or an acceleration of relativistic particles by passing of initial phase of a shock wave during the rising part of the flare and successive settling down of turbulence during decaying stage. The same shock then might be producing the radio emission, which is peaking  $\sim 60$  days later. For  $\gamma$ -ray flare of OJ 287, it was proposed that the flare is triggered by the interaction of moving blobs of plasma and the standing shock (Agudo et al. 2011). León-Tavares et al. (2012) observed the high spectral turnover frequencies in radio band. They suggested that such observations reveal the presence of emerging disturbances in the jet which are more likely to be responsible for the high flux states of the  $\gamma$ -ray emission.

We thank referee for her/his constructive comments which has significantly improved the manuscript. This work has made use of *Fermi* data, obtained from Fermi Science Support Center, provided by NASA's Goddard Space Flight Center (GSFC). The data, software and web tools obtained from NASA's High Energy Astrophysics Science Archive Research Center (HEASARC), a service of GSFC are used. The XRT Data Analysis Software (XRTDAS) developed under the responsibility of the ASI Science Data Center (ASDC), Italy has been used in this work. Also, data from the Steward Observatory spectropolarimetric monitoring project are used. This program is supported by Fermi Guest Investigator grants NNX08AW56G, NNX09AU10G, NNX12AO93G, and NNX15AU81G. In this research we used data from the OVRO 40-m monitoring program (Richards et al. 2011) which is supported in part by NASA grants NNX08AW31G, NNX11A043G, and NNX14AQ89G and NSF grants AST-0808050 and AST-1109911. We used Enrico, a community-developed Python package to simplify Fermi-LAT analysis (Sanchez & Deil 2013).

## REFERENCES

- Abdo, A. A., Ackermann, M., Ajello, M., et al. 2010a, *ApJS*, 188, 405, doi: [10.1088/0067-0049/188/2/405](https://doi.org/10.1088/0067-0049/188/2/405)
- . 2010b, *Nature*, 463, 919, doi: [10.1038/nature08841](https://doi.org/10.1038/nature08841)
- . 2011, *ApJL*, 733, L26, doi: [10.1088/2041-8205/733/2/L26](https://doi.org/10.1088/2041-8205/733/2/L26)
- Ackermann, M., Asano, K., Atwood, W. B., et al. 2010, *ApJ*, 716, 1178, doi: [10.1088/0004-637X/716/2/1178](https://doi.org/10.1088/0004-637X/716/2/1178)
- Agudo, I., Jorstad, S. G., Marscher, A. P., et al. 2011, *ApJL*, 726, L13, doi: [10.1088/2041-8205/726/1/L13](https://doi.org/10.1088/2041-8205/726/1/L13)
- Aller, H. D., Aller, M. F., & Hughes, P. A. 1985, *ApJ*, 298, 296, doi: [10.1086/163610](https://doi.org/10.1086/163610)
- Aller, M. F., Hughes, P. A., Aller, H. D., Latimer, G. E., & Hovatta, T. 2014, *ApJ*, 791, 53, doi: [10.1088/0004-637X/791/1/53](https://doi.org/10.1088/0004-637X/791/1/53)
- An, T., Baan, W. A., Wang, J.-Y., Wang, Y., & Hong, X.-Y. 2013, *MNRAS*, 434, 3487, doi: [10.1093/mnras/stt1265](https://doi.org/10.1093/mnras/stt1265)
- Atwood, W. B., Abdo, A. A., Ackermann, M., et al. 2009, *ApJ*, 697, 1071, doi: [10.1088/0004-637X/697/2/1071](https://doi.org/10.1088/0004-637X/697/2/1071)
- Bhatta, G. 2017, *ApJ*, 847, 7, doi: [10.3847/1538-4357/aa86ed](https://doi.org/10.3847/1538-4357/aa86ed)
- Böttcher, M. 2007, *Ap&SS*, 309, 95, doi: [10.1007/s10509-007-9404-0](https://doi.org/10.1007/s10509-007-9404-0)

- Britto, R. J., Bottacini, E., Lott, B., Razzaque, S., & Buson, S. 2016, *ApJ*, 830, 162, doi: [10.3847/0004-637X/830/2/162](https://doi.org/10.3847/0004-637X/830/2/162)
- Burrows, D. N., Hill, J. E., Nousek, J. A., et al. 2005, *SSRv*, 120, 165, doi: [10.1007/s11214-005-5097-2](https://doi.org/10.1007/s11214-005-5097-2)
- Carnerero, M. I., Raiteri, C. M., Villata, M., et al. 2015, *MNRAS*, 450, 2677, doi: [10.1093/mnras/stv823](https://doi.org/10.1093/mnras/stv823)
- Cash, W. 1979, *ApJ*, 228, 939, doi: [10.1086/156922](https://doi.org/10.1086/156922)
- Celotti, A., & Ghisellini, G. 2008, *MNRAS*, 385, 283, doi: [10.1111/j.1365-2966.2007.12758.x](https://doi.org/10.1111/j.1365-2966.2007.12758.x)
- Cohen, M. 2017, *Galaxies*, 5, 12, doi: [10.3390/galaxies5010012](https://doi.org/10.3390/galaxies5010012)
- Dondi, L., & Ghisellini, G. 1995, *MNRAS*, 273, 583, doi: [10.1093/mnras/273.3.583](https://doi.org/10.1093/mnras/273.3.583)
- Edelson, R. A., & Krolik, J. H. 1988, *ApJ*, 333, 646, doi: [10.1086/166773](https://doi.org/10.1086/166773)
- Fan, J. H. 1999, *A&A*, 347, 419
- Fan, J. H., Tao, J., Qian, B. C., et al. 2006, *PASJ*, 58, 797, doi: [10.1093/pasj/58.5.797](https://doi.org/10.1093/pasj/58.5.797)
- Fan, J. H., Yang, J. H., Liu, Y., et al. 2016, *ApJS*, 226, 20, doi: [10.3847/0067-0049/226/2/20](https://doi.org/10.3847/0067-0049/226/2/20)
- Ghisellini, G., Tavecchio, F., Foschini, L., et al. 2010, *MNRAS*, 402, 497, doi: [10.1111/j.1365-2966.2009.15898.x](https://doi.org/10.1111/j.1365-2966.2009.15898.x)
- Gorshkov, A. G., Ipatov, A. V., Ipatova, I. A., et al. 2009, *Astronomy Reports*, 53, 389, doi: [10.1134/S1063772909050023](https://doi.org/10.1134/S1063772909050023)
- Gorshkov, A. G., Ipatov, A. V., Konnikova, V. K., et al. 2014, *Astronomy Reports*, 58, 716, doi: [10.1134/S1063772914100060](https://doi.org/10.1134/S1063772914100060)
- Gorshkov, A. G., & Khromov, O. I. 1981, *Astrofizicheskie Issledovaniia Izvestiya Spetsial'noj Astrofizicheskoy Observatorii*, 14, 15
- Gorshkov, A. G., Konnikova, V. K., & Mingaliev, M. G. 2003, *Astronomy Reports*, 47, 903, doi: [10.1134/1.1626193](https://doi.org/10.1134/1.1626193)
- Hartman, R. C., Bertsch, D. L., Bloom, S. D., et al. 1999, *ApJS*, 123, 79, doi: [10.1086/313231](https://doi.org/10.1086/313231)
- Hewett, P. C., & Wild, V. 2010, *MNRAS*, 405, 2302, doi: [10.1111/j.1365-2966.2010.16648.x](https://doi.org/10.1111/j.1365-2966.2010.16648.x)
- Hong, X. Y., Jiang, D. R., Gurvits, L. I., et al. 2004, *A&A*, 417, 887, doi: [10.1051/0004-6361:20031784](https://doi.org/10.1051/0004-6361:20031784)
- Hovatta, T., Tornikoski, M., Lainela, M., et al. 2007, *A&A*, 469, 899, doi: [10.1051/0004-6361:20077529](https://doi.org/10.1051/0004-6361:20077529)
- Hovatta, T., Valtaoja, E., Tornikoski, M., & Lähteenmäki, A. 2009, *A&A*, 494, 527, doi: [10.1051/0004-6361:200811150](https://doi.org/10.1051/0004-6361:200811150)
- Hughes, P. A., Aller, H. D., & Aller, M. F. 1992, *ApJ*, 396, 469, doi: [10.1086/171734](https://doi.org/10.1086/171734)
- Hughes, P. A., Aller, M. F., & Aller, H. D. 2011, *ApJ*, 735, 81, doi: [10.1088/0004-637X/735/2/81](https://doi.org/10.1088/0004-637X/735/2/81)
- Kalberla, P. M. W., Burton, W. B., Hartmann, D., et al. 2005, *A&A*, 440, 775, doi: [10.1051/0004-6361:20041864](https://doi.org/10.1051/0004-6361:20041864)
- Lähteenmäki, A., & Valtaoja, E. 1999, *ApJ*, 521, 493, doi: [10.1086/307587](https://doi.org/10.1086/307587)



- Larionov, V. M., Villata, M., Raiteri, C. M., et al. 2016, *MNRAS*, 461, 3047, doi: [10.1093/mnras/stw1516](https://doi.org/10.1093/mnras/stw1516)
- León-Tavares, J., Valtaoja, E., Giommi, P., et al. 2012, *ApJ*, 754, 23, doi: [10.1088/0004-637X/754/1/23](https://doi.org/10.1088/0004-637X/754/1/23)
- León-Tavares, J., Valtaoja, E., Tornikoski, M., Lähteenmäki, A., & Nieppola, E. 2011, *A&A*, 532, A146, doi: [10.1051/0004-6361/201116664](https://doi.org/10.1051/0004-6361/201116664)
- Lister, M. L., & Homan, D. C. 2005, *AJ*, 130, 1389, doi: [10.1086/432969](https://doi.org/10.1086/432969)
- Liu, B., & Liu, X. 2014, *Ap&SS*, 352, 215, doi: [10.1007/s10509-014-1894-y](https://doi.org/10.1007/s10509-014-1894-y)
- Liu, F. K., Zhao, G., & Wu, X.-B. 2006a, *ApJ*, 650, 749, doi: [10.1086/507267](https://doi.org/10.1086/507267)
- Liu, Y., Jiang, D. R., & Gu, M. F. 2006b, *ApJ*, 637, 669, doi: [10.1086/498639](https://doi.org/10.1086/498639)
- Marscher, A. P., Jorstad, S. G., D’Arcangelo, F. D., et al. 2008, *Nature*, 452, 966, doi: [10.1038/nature06895](https://doi.org/10.1038/nature06895)
- Mattox, J. R., Bertsch, D. L., Chiang, J., et al. 1996, *ApJ*, 461, 396, doi: [10.1086/177068](https://doi.org/10.1086/177068)
- Max-Moerbeck, W., Hovatta, T., Richards, J. L., et al. 2014, *MNRAS*, 445, 428, doi: [10.1093/mnras/stu1749](https://doi.org/10.1093/mnras/stu1749)
- Mukherjee, R., Bertsch, D. L., Bloom, S. D., et al. 1997, *ApJ*, 490, 116, doi: [10.1086/304851](https://doi.org/10.1086/304851)
- Planck Collaboration, Ade, P. A. R., Aghanim, N., et al. 2014, *A&A*, 571, A16, doi: [10.1051/0004-6361/201321591](https://doi.org/10.1051/0004-6361/201321591)
- Poole, T. S., Breeveld, A. A., Page, M. J., et al. 2008, *MNRAS*, 383, 627, doi: [10.1111/j.1365-2966.2007.12563.x](https://doi.org/10.1111/j.1365-2966.2007.12563.x)
- Raiteri, C. M., Villata, M., Aller, H. D., et al. 2001, *A&A*, 377, 396, doi: [10.1051/0004-6361:200111112](https://doi.org/10.1051/0004-6361:200111112)
- Raiteri, C. M., Villata, M., Larionov, V. M., et al. 2008, *A&A*, 491, 755, doi: [10.1051/0004-6361:200810869](https://doi.org/10.1051/0004-6361:200810869)
- Raiteri, C. M., Villata, M., Acosta-Pulido, J. A., et al. 2017, *Nature*, 552, 374, doi: [10.1038/nature24623](https://doi.org/10.1038/nature24623)
- Ramakrishnan, V., León-Tavares, J., Rastorgueva-Foi, E. A., et al. 2014, *MNRAS*, 445, 1636, doi: [10.1093/mnras/stu1873](https://doi.org/10.1093/mnras/stu1873)
- Richards, J. L. 2012, PhD thesis, California Institute of Technology
- Richards, J. L., Hovatta, T., Max-Moerbeck, W., et al. 2014, *MNRAS*, 438, 3058, doi: [10.1093/mnras/stt2412](https://doi.org/10.1093/mnras/stt2412)
- Richards, J. L., Max-Moerbeck, W., Pavlidou, V., et al. 2011, *ApJS*, 194, 29, doi: [10.1088/0067-0049/194/2/29](https://doi.org/10.1088/0067-0049/194/2/29)
- Rolke, W. A., López, A. M., & Conrad, J. 2005, *Nuclear Instruments and Methods in Physics Research A*, 551, 493, doi: [10.1016/j.nima.2005.05.068](https://doi.org/10.1016/j.nima.2005.05.068)
- Roming, P. W. A., Kennedy, T. E., Mason, K. O., et al. 2005, *SSRv*, 120, 95, doi: [10.1007/s11214-005-5095-4](https://doi.org/10.1007/s11214-005-5095-4)
- Sanchez, D. A., & Deil, C. 2013, ArXiv e-prints. <https://arxiv.org/abs/1307.4534>

- Savolainen, T., & Kovalev, Y. Y. 2008, *A&A*, 489, L33, doi: [10.1051/0004-6361:200810423](https://doi.org/10.1051/0004-6361:200810423)
- Schlafly, E. F., & Finkbeiner, D. P. 2011, *ApJ*, 737, 103, doi: [10.1088/0004-637X/737/2/103](https://doi.org/10.1088/0004-637X/737/2/103)
- Schneider, D. P., Richards, G. T., Hall, P. B., et al. 2010, *AJ*, 139, 2360, doi: [10.1088/0004-6256/139/6/2360](https://doi.org/10.1088/0004-6256/139/6/2360)
- Shaw, M. S., Romani, R. W., Cotter, G., et al. 2012, *ApJ*, 748, 49, doi: [10.1088/0004-637X/748/1/49](https://doi.org/10.1088/0004-637X/748/1/49)
- Shukla, A., Mannheim, K., Patel, S. R., et al. 2018, *ApJL*, 854, L26, doi: [10.3847/2041-8213/aaacca](https://doi.org/10.3847/2041-8213/aaacca)
- Sillanpaa, A., Haarala, S., Valtonen, M. J., Sundelius, B., & Byrd, G. G. 1988, *ApJ*, 325, 628, doi: [10.1086/166033](https://doi.org/10.1086/166033)
- Simonetti, J. H., Cordes, J. M., & Heeschen, D. S. 1985, *ApJ*, 296, 46, doi: [10.1086/163418](https://doi.org/10.1086/163418)
- Smith, P. S., Montiel, E., Rightley, S., et al. 2009, ArXiv e-prints, <https://arxiv.org/abs/0912.3621>
- Steffen, W., Zensus, J. A., Krichbaum, T. P., Witzel, A., & Qian, S. J. 1995, *A&A*, 302, 335
- Thompson, D. J., Bertsch, D. L., Dings, B. L., et al. 1995, *ApJS*, 101, 259, doi: [10.1086/192240](https://doi.org/10.1086/192240)
- Urry, C. M., & Padovani, P. 1995, *PASP*, 107, 803, doi: [10.1086/133630](https://doi.org/10.1086/133630)
- Valtaoja, E., Lähteenmäki, A., Teräsranta, H., & Lainela, M. 1999, *ApJS*, 120, 95, doi: [10.1086/313170](https://doi.org/10.1086/313170)
- Valtaoja, E., Teräsranta, H., Tornikoski, M., et al. 2000, *ApJ*, 531, 744, doi: [10.1086/308494](https://doi.org/10.1086/308494)
- Villata, M., & Raiteri, C. M. 1999, *A&A*, 347, 30
- Wang, J.-Y., An, T., Baan, W. A., & Lu, X.-L. 2014, *MNRAS*, 443, 58, doi: [10.1093/mnras/stu1135](https://doi.org/10.1093/mnras/stu1135)
- Welsh, W. F. 1999, *PASP*, 111, 1347, doi: [10.1086/316457](https://doi.org/10.1086/316457)
- Wills, B. J., Pollock, J. T., Aller, H. D., et al. 1983, *ApJ*, 274, 62, doi: [10.1086/161426](https://doi.org/10.1086/161426)
- Xie, G. Z., Yi, T. F., Li, H. Z., Zhou, S. B., & Chen, L. E. 2008, *AJ*, 135, 2212, doi: [10.1088/0004-6256/135/6/2212](https://doi.org/10.1088/0004-6256/135/6/2212)
- Xie, G. Z., Zhou, S. B., & Liang, E. W. 2004, *AJ*, 127, 53, doi: [10.1086/380218](https://doi.org/10.1086/380218)
- Xiong, D. R., & Zhang, X. 2014, *MNRAS*, 441, 3375, doi: [10.1093/mnras/stu755](https://doi.org/10.1093/mnras/stu755)